minerals

MDPI

Communication

Synthesis of Geopolymers Based on Fractionated Class F and Class C Fly Ashes with Preliminary Removal of the Iron-Containing Magnetic Component

Alexander M. Kalinkin [1,*], Elena V. Fomenko [2], Elena V. Kalinkina [1], Ekaterina A. Kruglyak [1], Alla G. Ivanova [1] and Galina V. Akimochkina [2]

[1] Tananaev Institute of Chemistry—Subdivision of the Federal Research Centre "Kola Science Centre of the Russian Academy of Sciences", Akademgorodok 26a, Apatity184209, Russia
[2] Institute of Chemistry and Chemical Technology SB RAS, Federal Research Center ''Krasnoyarsk Science Center SB RAS", Akademgorodok 50/24, Krasnoyarsk 660036, Russia; fom@icct.ru (E.V.F.)
* Correspondence: a.kalinkin@ksc.ru

Abstract

The utilization of fly ash (FA) remains an urgent environmental and resource-related challenge, and geopolymerization is regarded as a promising route for incorporating large quantities of FA into the production of construction materials. The aim of this study was to investigate the feasibility of producing a geopolymer binder based on pre-fractionated Class F and Class C FAs without mechanical activation, as well as to assess the effect of removing the iron-containing magnetic component on the reactivity of Class F FA and the strength of the resulting geopolymer. A fine fraction was separated from low-calcium Class F FA, and its magnetic component was removed by dry magnetic separation. The resulting non-magnetic fraction, accounting for 80% of the fine fraction, was mixed with a fine fraction of high-calcium Class C FA at a ratio of 80:20. Geopolymerization was carried out using a sodium hydroxide solution, followed by thermal curing. Compared with the raw Class F FA, separation of the fine non-magnetic fraction increased the geopolymer strength by factors of 5.5 (9.9 ± 1.0 vs. 1.8 ± 0.3 MPa), 6.0 (12.6 ± 1.3 vs. 2.1 ± 0.4 MPa), and 4.9 (15.2 ± 1.5 vs. 3.1 ± 0.4 MPa) after 7, 28, and 180 days, respectively. Further addition of the fine Class C FA fraction increased the strength by factors of 2.9 (28.5 ± 1.4 vs. 9.9 ± 1.0 MPa), 2.4 (30.3 ± 1.5 vs. 12.6 ± 1.3 MPa), and 2.2 (32.9 ± 1.6 vs. 15.2 ± 1.5 MPa) after 7, 28, and 180 days, respectively. The formation of an N-(C)-A-S-H gel and a new crystalline phase—katoite—was observed. The proposed approach makes it possible to obtain geopolymers with strengths comparable to those of geopolymers based on mechanically activated, unfractionated FAs while avoiding the energy-intensive milling step and enabling the comprehensive utilization of FA.

Keywords: geopolymers; low calcium fly ash; high calcium fly ash; blending; fractionation; magnetic separation

Academic Editor: Abbas Taheri

Received: 22 October 2026
Revised: 15 November 2026
Accepted: 21 November 2026
Published: 24 November 2026

Copyright: © 2026 by the authors. Licensee MDPI, Basel, Switzerland. This article is an open access article distributed under the terms and conditions of the Creative Commons Attribution (CC BY) license.

1. Introduction

The utilization of coal fly ash (FA), generated in large quantities during coal combustion, is an important environmental and resource-related challenge [1]. One promising approach for FA utilization is its use as an aluminosilicate precursor for the production of

geopolymer binders [2–4]. Compared with Portland cement production, geopolymer synthesis does not require limestone decarbonization and can generally be carried out at substantially lower processing temperatures, making geopolymers a potentially more environmentally sustainable alternative to conventional cementitious materials [4].

Depending on their chemical and mineralogical composition, FAs can differ significantly in their reactivity under alkaline conditions, which should be considered when selecting an alkali activator, a geopolymer formulation, and curing conditions [5,6]. In particular, low-calcium Class F and high-calcium Class C FAs can be used either individually or in combination for geopolymer production [7–12]. Each type of FA, however, has specific advantages and limitations. Low-calcium Class F FA contains a sufficient amount of amorphous aluminosilicate phase (glass phase) required for the synthesis of N-A-S-H gel—the main binding phase in geopolymers. In contrast, high-calcium Class C FA contains reactive CaO and other calcium-containing phases that can accelerate the dissolution of Class F FA and enhance the performance of the alkali-activated binder [11].

High-calcium FA generally exhibits higher reactivity and faster setting, but the use of this FA as the sole aluminosilicate precursor may be associated with the rapid setting of the geopolymer mixture, adversely affecting its workability. In such cases, an increase in the water-to-solid ratio or the addition of specialized admixtures may be required to ensure adequate workability [13,14]. However, excessive liquid content can increase the porosity of the hardened binder and consequently reduce its mechanical strength [14,15]. In addition, high-calcium FA-based geopolymer systems can exhibit substantial heat evolution during the early stages of geopolymerization. The resulting temperature rise may affect the development of the microstructure and, under unfavorable conditions, promote microcrack formation, impairing the physical and mechanical properties of the hardened binder [8,16].

One of the main limitations of low-calcium FAs is that they may exhibit relatively low reactivity during geopolymerization, particularly under ambient curing conditions [17,18]. Various approaches have therefore been employed to enhance their reactivity, including mechanical activation [19–23] and the incorporation of controlled amounts of calcium-containing components, such as blending with high-calcium FA as an additional calcium source [11,12,24–26]. This complementary use of Class F and Class C FAs can effectively improve overall reactivity and performance by leveraging the beneficial characteristics of each. Additionally, the separation or classification of fine fractions from the raw FA is another promising approach. Such fractions may exhibit higher reactivity due to their smaller particle size, greater specific surface area, and differences in glass content and chemical/mineralogical characteristics [13,27–32].

In our previous study [33], geopolymer synthesis was investigated using a mixture of Class F FA and a Class C FA containing 41.58 wt% CaO. The objective was to increase the compressive strength of the geopolymers by combining FAs with low and very high calcium contents and to investigate the effect of intensive mechanical activation of the starting materials in a planetary mill on geopolymer synthesis. A sodium hydroxide solution was used as the alkaline activator, and curing was performed using thermal treatment. Replacing 20% of the low-calcium FA with high-calcium FA substantially increased the compressive strength of the geopolymers [33].

However, FA is commonly used for geopolymer production as received, without preliminary separation into individual components. Such an approach does not fully account for the complex and heterogeneous nature of FA and the potential for selectively recovering valuable constituents from this secondary raw material. In particular, a substantial proportion of iron in FA is associated with magnetic iron-bearing phases, predominantly magnetite and other iron oxides, providing an opportunity for their separation by magnetic methods [31,34]. The resulting iron-enriched magnetic fraction can be regarded as a

potentially valuable secondary resource for metallurgical and other applications [34]. The non-magnetic fraction, enriched in aluminosilicate components, can be further processed, including for the production of geopolymer binders [31,34]. Furthermore, the removal of the magnetic fraction may alter the chemical and mineralogical composition of the remaining aluminosilicate material and, consequently, increase its reactivity during geopolymerization [32].

As a continuation of our previous work [33], in this article, to prepare geopolymers without the use of mechanical activation, a fine fraction was first separated from the same Class F FA, from which a magnetic fraction was then separated by dry magnetic separation as a fraction enriched in iron. The non-magnetic part of the fine fraction (80%) was mixed with the fine fraction of Class C FA (20%), without the use of mechanical activation, and served as the precursor for geopolymer synthesis under the same preparation and curing conditions as in the previous article [33]. The results show that the proposed approach yields geopolymers with strengths comparable to those of geopolymers produced from a mechanically activated FA mixture without fractionation. This approach offers a means of avoiding the energy-intensive milling step while maintaining performance and enabling more rational and comprehensive utilization of FA.

2. Materials and Methods

In this work, we used fine fractions separated from the same FAs as in our previous study [33] as precursors for the preparation of geopolymers: low-calcium FA (Class F FA) from Apatity Thermal Power Plant (Apatity, Murmansk Region, Russia) and high-calcium FA (Class C FA) from Krasnoyarsk Thermal Power Plant 2 (Krasnoyarsk, Russia). The Class F FA comprises a ferruginous aluminosilicate glass phase and crystalline phases including quartz, mullite, magnetite, and hematite. In addition to its glass phase, the Class C FA contains calcium-rich crystalline phases such as tricalcium aluminate ($Ca_3Al_2O_6$), alumino-substituted calcium ferrite ($Ca_2(Al,Fe)O_5$), calcium sulfate, carbonate, hydroxide, and oxide, along with quartz, periclase, and iron-containing spinel. Detailed characterization of these FAs, including particle size distribution, is provided in [33].

The fine fraction of low-calcium FA, hereinafter referred to as F-S, was prepared as follows: Firstly, fraction with particle size less than 20 μm was separated using a sieving method. The content of this fraction in the low-calcium FA was 66 wt %. Subsequently, the magnetic components were separated from this fraction by dry magnetic separation using a neodymium magnet (NdFeB, F = 24 lb). The content of the magnetic component in this fraction was 6 wt. %. It should be noted that the fine fraction before magnetic separation is an intermediate stream rather than a target product. The separated magnetic fraction was designated as F-MF-S. The resulting non-magnetic fine fraction, which accounted for 62 wt % of the initial low-calcium FA, was then used as a precursor for geopolymer synthesis. Fine fraction of Class C FA was obtained by aerodynamic separation (fraction C-S) [35]. Table 1 presents the chemical compositions of the fine fractions compared with those of the raw ashes. The chemical compositions of F, C, and C-S were determined by wet chemical analysis, and those of F-S and F-MF-S by SEM-EDS (Hitachi TM-4000 microscope, High Technologies Corporation, Hitachi, Tokyo, Japan). In all cases, oxide contents are normalized to 100% on an LOI-free basis, while LOI is reported separately and is not included in the normalization.

Table 1. Chemical compositions of the raw low-calcium FA (F), high-calcium FA (C) [33], and corresponding fine fractions—F-S, F-MF-S and C-S (wt %) *.

Precursor	SiO_2	Al_2O_3	Fe_2O_3	CaO	MgO	Na_2O	K_2O	TiO_2	MnO	SO_3	LOI
F-S	56.7	25.0	5.4	7.3	1.5	0.1	2.3	1.0	0.10	0.6	1.86
F-MF-S	20.9	10.7	56.0	5.1	5.0	0.5	0.5	0.4	0.5	0.4	–
F	56.28	22.85	8.83	6.13	2.18	0.86	1.30	1.0	0.09	0.48	3.02
C-S	16.9	8.9	14.6	41.9	8.8	0.32	0.15	0.27	–	8.11	5.50
C	22.3	7.7	13.9	41.6	8.5	0.25	0.50	0.27	–	5.12	3.30

* Oxide contents are normalized to 100% on an LOI-free basis.

To evaluate the efficiency of the dry magnetic separation technique, the following technological parameters of iron enrichment [36,37] were calculated:

$$\gamma_c = 100 \times (\alpha - \theta)/(\beta - \theta), \quad (1)$$

where γ_c is the iron concentrate yield (%); α, β, θ are the concentrations of Fe_2O_3 in the raw ash F, magnetic fraction F-MF-S, and non-magnetic F-S fraction, respectively (%).

$$\varepsilon = \gamma_c \times \beta / \alpha, \quad (2)$$

where ε is the iron recovery (%).

$$E = (\varepsilon - \gamma_c)/(100 - \alpha) \times 100, \quad (3)$$

where E is the enrichment efficiency (%).

Geopolymers were prepared from blend of F-S and C-S, with 100% F-S and 100% raw Class F FA serving as the controls. The blend ratio matched that in our recent study on geopolymers based on mechanically activated Class F and Class C FA [33]: 80% F-S + 20% C-S, designated as F_8C_2-S. The geopolymer specimen size, alkaline activator, and curing conditions were also identical to those in [33]. Pastes were made by hand-mixing FA with 8.3 M NaOH until a plastic consistency was obtained, with the Na_2O content fixed at 6% of the FA mass (Na_2O/FA mass ratio = 0.06). To prepare the geopolymer paste, 299.3 g of 8.3 M NaOH solution was required per 1000 g of FA (or FA blend). The water content was adjusted to maintain consistent workability, and the water-to-solid (*w*/*s*) ratio was calculated as the total water mass divided by the FA mass. In this study, the performance of geopolymers is compared at a constant Na_2O/FA ratio, rather than at a constant *w*/*s* ratio. Table 2 presents the mixture design used for geopolymer preparation, including those used as control samples prepared in [33] and cured under the same conditions (please refer to the "Abbreviation" section for geopolymer code designations). Cubes (1.41 × 1.41 × 1.41 cm) were molded, steam-cured at 80–85 °C for 8 h, and then cured in ambient air at 95%–100% RH and 20 ± 2 °C until testing. Compression tests were performed on three cubes for each curing age, cast from a single batch, using a PGM-100MG4-A hydraulic press. The geopolymers prepared using F-S and F_8C_2-S are denoted as GF-S and GF_8C_2-S, respectively.

Table 2. The compositions of mixtures employed in geopolymer synthesis (MA—mechanical activation time; S_{sp}—BET specific surface area of the precursor; Na_2O/FA—Na_2O content in NaOH relative to the mass of FA; *w*/*s*—water-to-solid ratio).

Geopolymer Code	F (wt.%)	F-S (wt.%)	C (wt.%)	C-S (wt.%)	MA (s)	S_{sp} (m^2/g)	NaOH (M)	Na_2O/FA (wt.%)	*w*/*s*
GF-0	100	0	0	0	0	1.29	8.3	6	0.28
GF-S	0	100	0	0	0	2.52	8.3	6	0.39
GF_8C_2-S	0	80	0	20	0	3.56	8.3	6	0.37

GF-30 *	100	0	0	0	30	2.66	8.3	6	0.31
GF-180 *	100	0	0	0	180	8.26	8.3	6	0.32
GF_8C_2-30 *	80	0	20	0	30	4.00	8.3	6	0.31
GF_8C_2-180 *	80	0	20	0	180	5.85	8.3	6	0.35

* geopolymers prepared in [33].

X-ray diffraction (XRD) measurements were performed with Rigaku Miniflex-600 diffractometer (Rigaku Corporation, Tokyo, Japan) using Cu Kα radiation at a scan rate of 2° (2θ) min^{-1}. FTIR spectra were recorded on a Nicolet 6700 FTIR spectrometer (Thermo Fisher Scientific, Madison, WI, USA) using potassium bromide (KBr) pellets. SEM-EDS characterization was carried out with Hitachi TM-4000 microscope (High Technologies Corporation, Hitachi, Tokyo, Japan). Specific surface area was determined with a Micromeritics FlowSorb 2300 instrument (Micromeritics Instrument Corp., Norcross, GA, USA) via the single-point BET method, using N_2 as the adsorbate gas. Particle-size distributions were measured in wet mode with a MicroTec 22 laser diffractometer (Fritsch GmbH, Idar-Oberstein, Germany).

3. Results and Discussion

3.1. Magnetic Separation: Efficiency and Product Characterization

The efficiency of magnetic separation, as with any beneficiation process, is evaluated using several parameters [36–39]. The key parameters used to assess the completeness of recovery and the quality of the resulting concentrate include the content of the target component in the feed and separation products, the product yields, the recovery of the components into the separation products, and the separation efficiency. For fly ash, iron recovery is complicated by the low content of the magnetic fraction and the fine particle size. According to [38], conventional dry magnetic separation methods used to extract magnetic concentrate from fly ash provide enrichment efficiencies ranging from 8% to 22%. Table 3 presents a comparison between the iron magnetic separation efficiencies reported in the literature [38,39] and those obtained in this study for low-calcium FA. It should be emphasized that the present study employed dry magnetic separation, in contrast to the wet separation data reported in [39].

Table 3. Iron recovery efficiency achieved in the present study compared with various separation methods reported in the literature [38,39].

Separation Techniques	β (%)	γ_c (%)	ε (%)	E (%)	Reference
Particle-size and dry magnetic separation	56.0	6.5	41.8	38.7	Present study
Particle-size and dry magnetic separation	59.1	2.9	–	27.3	[38]
Dry magnetic separation: 1-stage	9.3	0.5	0.48	0.2	[39]
Dry magnetic separation: 2-stage	11.4	33.7	72.6	41.1	[39]
Wet magnetic separation	12.7	30.3	73.2	45.2	[39]

For the combined method of "particle-size fractionation + magnetic separation" used in the present study, the enrichment efficiency was 38.7%. A method of similar type from [38], which integrates the removal of coarse aggregates by sieving and a spiral dry magnetic separation technique, shows a lower value of this parameter (27.3%). For the methods from [39], the beneficiation parameters differ substantially: one-stage dry magnetic separation exhibits an extremely low enrichment efficiency, whereas two-stage separation and wet magnetic separation markedly improve the recovery parameters. However, the iron content in magnetic fractions was in all cases lower [39] than that in the methods involving preliminary particle-size fractionation [38].

The SEM images (Figure 1) reveal distinct differences in the morphology of the magnetic and non-magnetic fractions.

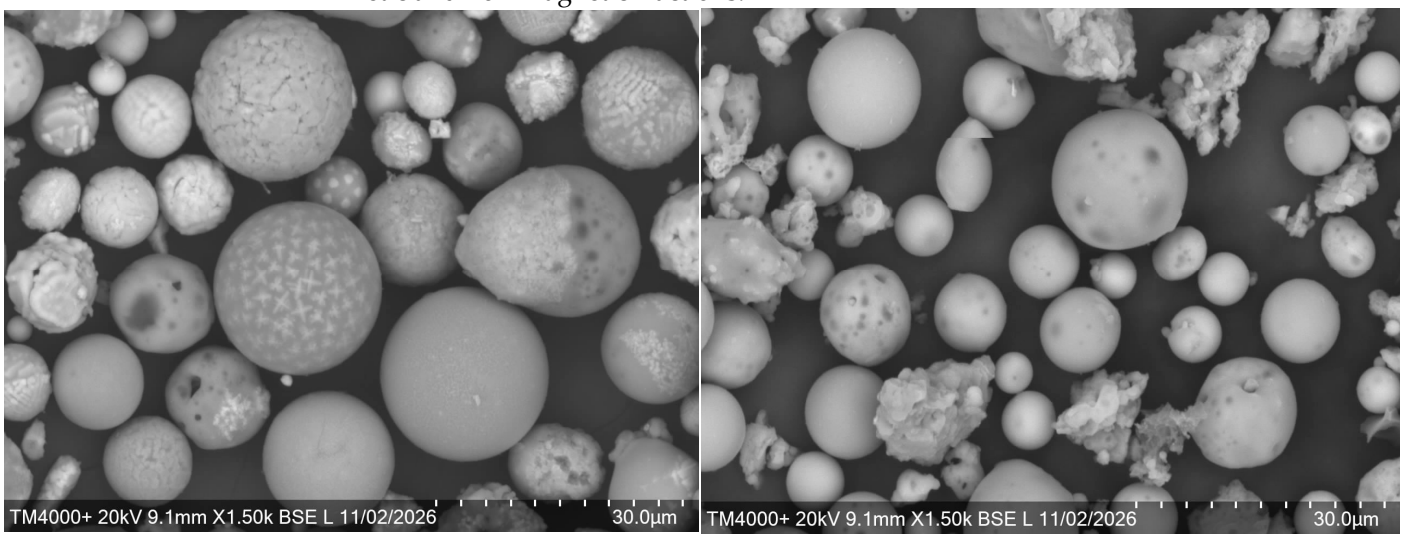

(**a**) (**b**)

Figure 1. SEM images of magnetic F-MF-S (**a**) and non-magnetic F-S (**b**) fractions.

The magnetic fraction (F-MF-S, Figure 1a) contains a significantly higher proportion of rough-surfaced particles. Many spherical particles in this fraction exhibit rough, spotted, or skeletal surfaces (e.g., the large microsphere in the center), indicating the presence of iron-bearing phases (such as magnetite) either on the surface or within the particle structure. The presence of these irregular and rough particles is attributed to the iron-containing minerals, allowing them to be separated by magnetic separation. In contrast, the non-magnetic fraction (F-S, Figure 1b) consists predominantly of smooth, spherical aluminosilicate microspheres of varying sizes, which are typical of the glass phase of fly ash. The surfaces of most microspheres are relatively clean and smooth, and irregular, rough particles are present only in minor amounts.

The difference in the overall composition is evident in Figure 2, where the SEM images are supplemented with element distribution maps and energy-dispersive spectra.

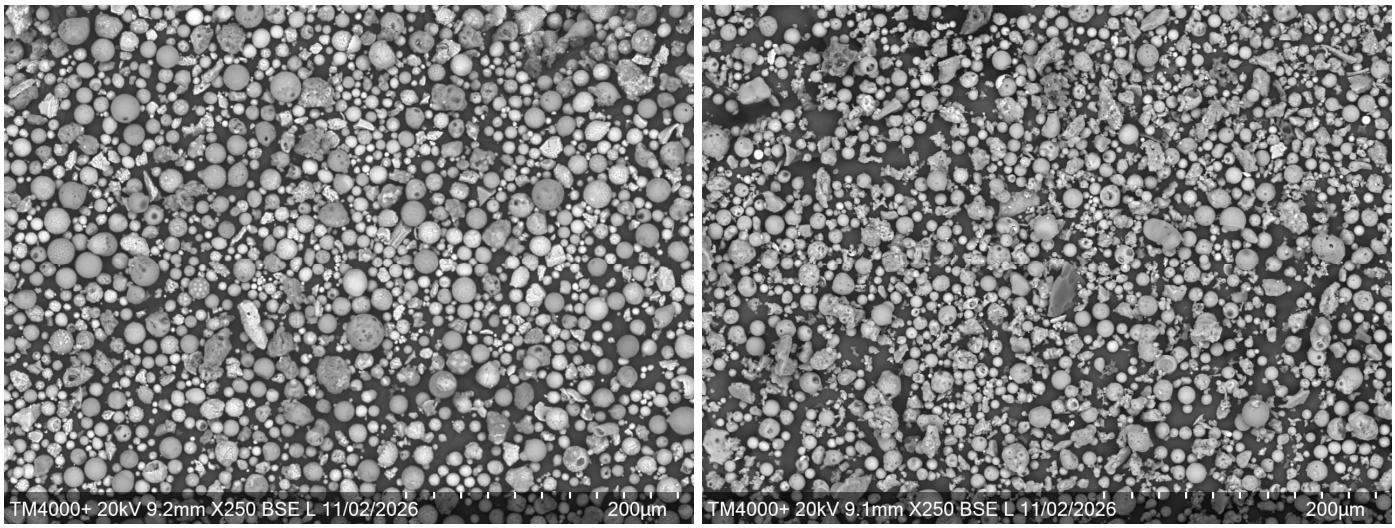

(**a**) (**b**)

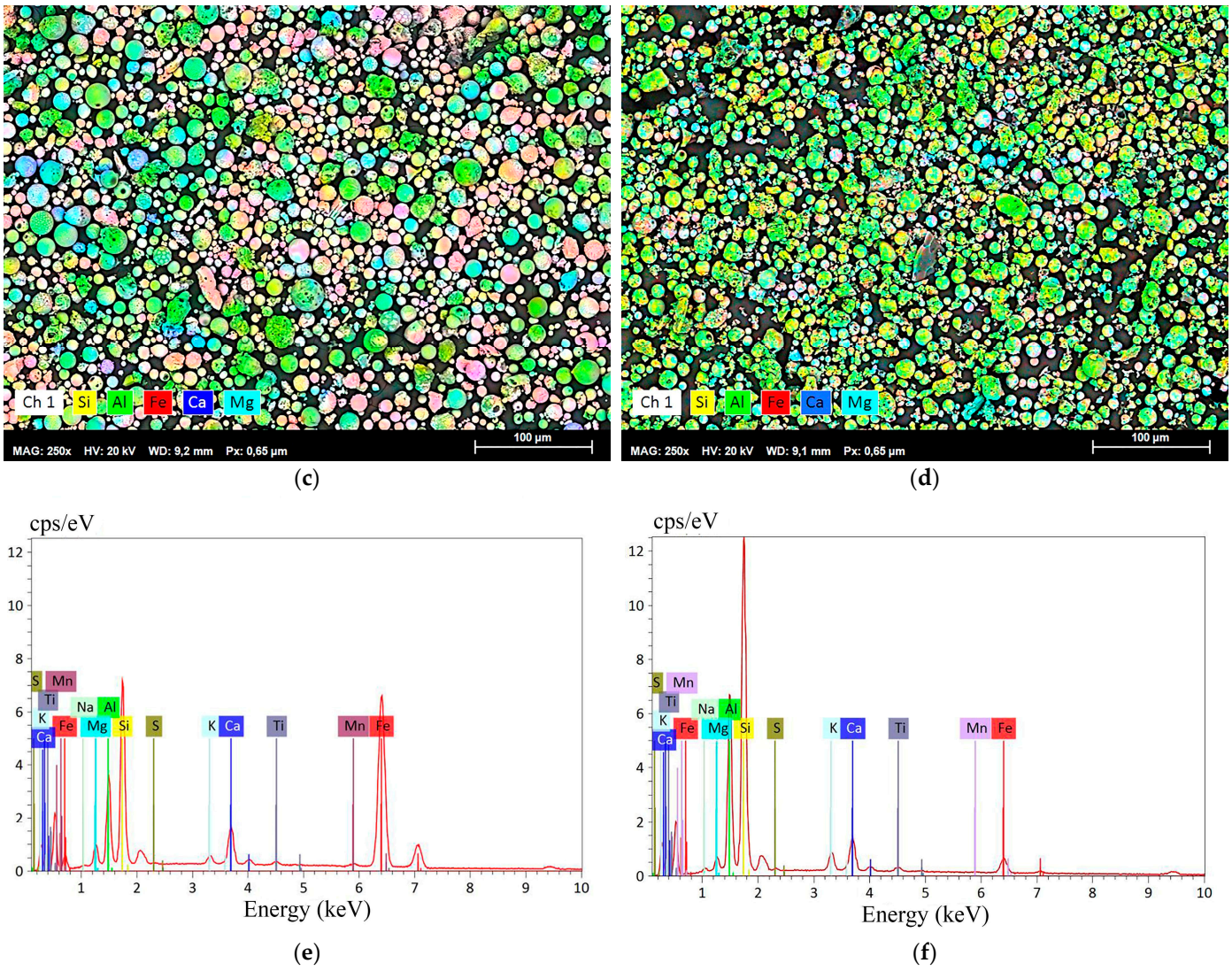

Figure 2. SEM images (**a**,**b**), elemental distribution maps (**c**,**d**), energy-dispersive spectra (**e**,**f**) for magnetic F-MF-S (**a**,**c**,**e**) and non-magnetic F-S (**b**,**d**,**f**) fractions.

The elemental maps (Figure 2c,d) reveal the key compositional difference. In the magnetic fraction (left), iron (red) is widely distributed and strongly correlates with the bright particles and the skeletal/spotted structures on the microspheres, indicating the presence of iron-bearing phases. In the non-magnetic fraction (right), the red signal is significantly weaker and localized, while the signal from silicon (green) and aluminum (light blue/green) strongly dominates the matrix, confirming the aluminosilicate nature of this fraction.

The spectra corroborate the mapping data (Figure 2e,f). The magnetic fraction (left) shows a very prominent and intense Fe peak (red) at approximately 6.4 keV, comparable in intensity to the Si and Al peaks. In contrast, the non-magnetic fraction (right) is characterized by dominant Si and Al peaks, with only a minor Fe peak. This directly confirms that the dry magnetic separation successfully concentrated the iron-bearing phases into the magnetic fraction.

According to the XRD data, the magnetic fraction (F-MF-S) is composed of magnetite, hematite, and quartz (Figure 3). The presence of intense magnetite reflections confirms that it is the predominant iron-bearing phase, while hematite is present in subordinate amounts.

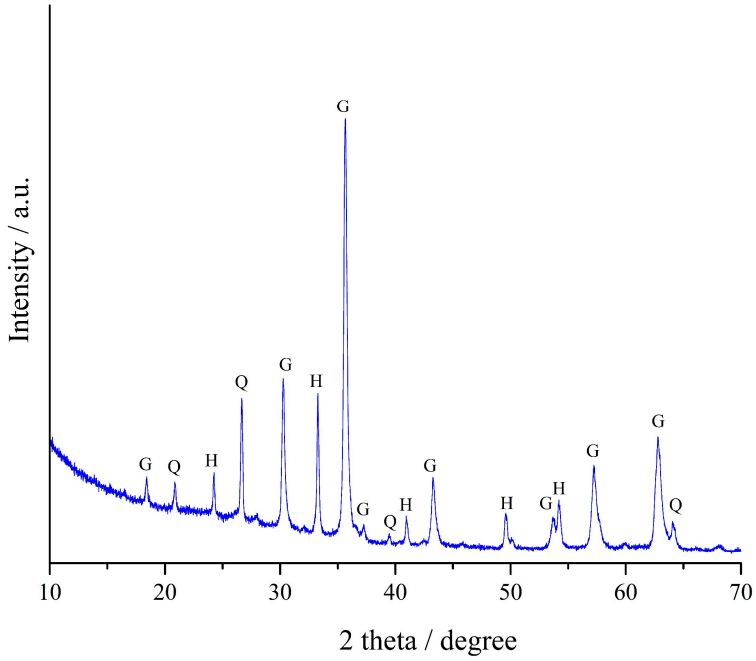

Figure 3. XRD patterns of magnetic F-MF-S fraction. The marked phases are: Q—α-quartz (PDF 00-046-1045), G—magnetite (PDF 04-007-2412), and H—hematite (PDF 00-033-0664).

Figure 4 shows SEM images of individual microspheres (a, b, c) from the magnetic fraction F-MF-S. All three microspheres exhibit a distinct spherical shape but differ noticeably in their surface morphology. Microsphere (a) has a relatively smooth surface with characteristic spotted or skeletal patterns, which likely represent fine iron-bearing crystalline inclusions (such as magnetite) embedded in the glassy matrix. Microsphere (b) shows a rougher, more granular surface with irregular crusts, indicating a higher degree of surface crystallization. Microsphere (c) displays pronounced, intersecting polygonal cracks on its surface. The presence of these diverse morphologies, particularly the spotted patterns and rough surfaces, confirms that iron-bearing phases are heterogeneously distributed on and within the magnetic microspheres.

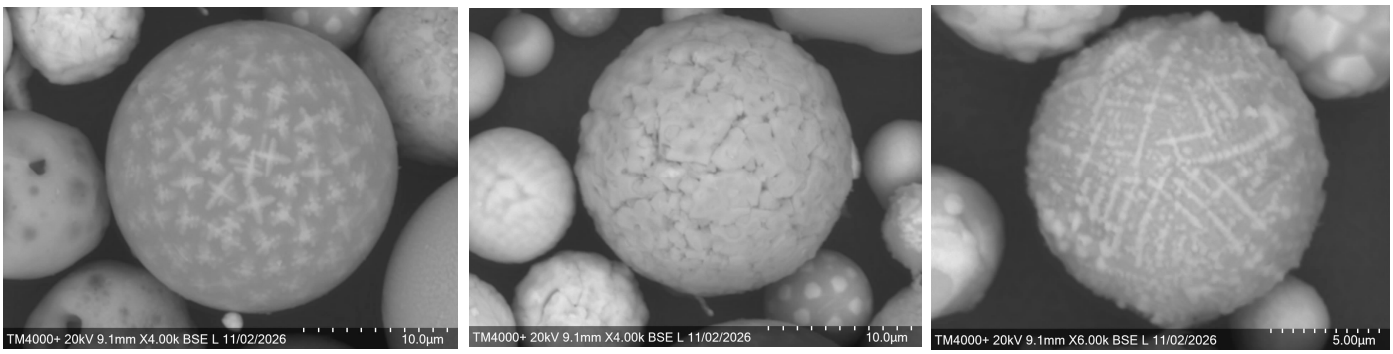

(**a**) (**b**) (**c**)

Figure 4. SEM images of individual microspheres from magnetic fraction F-MF-S, showing diverse morphologies: (**a**) a relatively smooth surface with characteristic spotted or skeletal patterns; (**b**) a rougher, more granular surface with irregular crusts; and (**c**) a surface with pronounced intersecting polygonal cracks.

Table 4 presents the chemical composition of individual microspheres (a, b, and c) from the magnetic fraction F-MF-S (Figure 4), as determined by EDS analysis. The data reveal significant heterogeneity in the composition of the magnetic microspheres. Microsphere (a) contains a noticeable amount of aluminosilicates, as indicated by its high SiO_2

and Al_2O_3 contents; however, its iron content is also substantial. Notably, it also contains a relatively high amount of MgO. In sharp contrast, microspheres (b) and (c) are highly enriched in iron. Their Fe content is dominant, while their aluminosilicate content is significantly lower compared to microsphere (a). This indicates that these microspheres are predominantly composed of iron-bearing phases with minimal aluminosilicate glass. Additionally, microsphere (b) exhibits an elevated MgO content, which, together with high iron, suggests the presence of an iron–magnesium spinel phase (such as magnesioferrite or a magnetite–magnesioferrite solid solution).

Table 4. Chemical composition (wt %) of individual microspheres from magnetic fraction F-MF-S (Figure 4) based on EDS data.

Reference Microsphere	SiO_2	Al_2O_3	Fe_2O_3	CaO	MgO	Na_2O	K_2O	TiO_2	MnO	SO_3
a	34.04	15.05	30.30	1.25	9.73	0.25	4.72	4.30	0.16	0.20
b	5.04	3.91	67.98	3.64	18.18	0.13	0.21	0.15	0.62	0.15
c	20.56	10.56	61.81	4.47	0.73	0.23	0.73	0.43	0.34	0.14

3.2. Characterization of Geopolymer Precursors

Figure 5 shows the XRD patterns and FTIR spectra of the fine fraction of low-calcium FA (F-S) and the raw FA (F). Overall, the phase assemblage of F-S was consistent with that of F and included a glass phase, as well as quartz, mullite, magnetite, and hematite [33]. As clearly seen in Figure 5a, compared with F, the intensities of the magnetite reflections in the XRD pattern of F-S were substantially reduced as a result of magnetic separation. This is consistent with Table 1, which shows that relative to the raw FA, the Fe_2O_3 content of the F-S fraction decreased by 3.3 wt %, whereas its SiO_2 and Al_2O_3 contents increased by 1.4 wt % and 2.5 wt %, respectively.

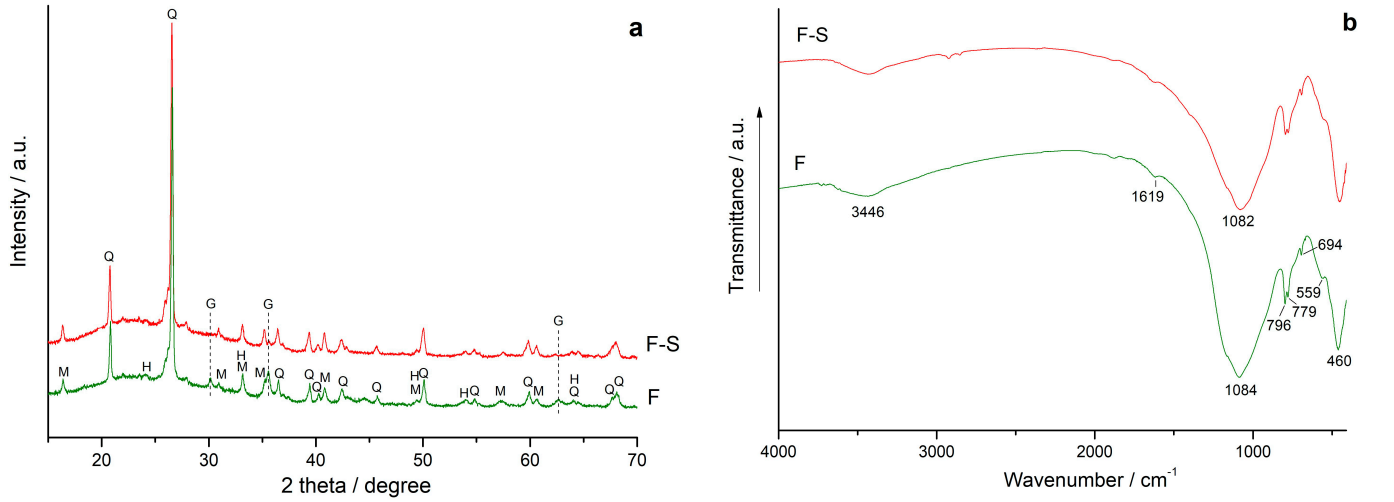

Figure 5. XRD patterns (**a**) and FTIR spectra (**b**) of the raw Class F FA (F) and fine fraction of Class F FA (F-S). The marked phases are: Q—α-quartz (PDF 00-046-1045), M—mullite (PDF 01-089-2644), G—magnetite (PDF 04-007-2412), and H—hematite (PDF 00-033-0664).

As shown in Figure 5b, the FTIR spectra of F-S and F are nearly identical. Atmospheric water absorption on the FA surface is manifested by bands at 3446 and 1619 cm^{-1}, assigned to O–H stretching and H–O–H bending modes, respectively. The strongest broad band at 1084–1082 cm^{-1} is assigned to the asymmetric stretching vibrations of Si–O–T (T = Si, Al) in the glass phase of the FA, α-quartz, and mullite. The bands at 796, 779, and 694 cm^{-1}, corresponding to the symmetric stretching vibrations of Si–O–Si, together with the

band at 460 cm^{-1}, corresponding to Si–O–Si bending vibrations, are attributed to α-quartz. The band at 559 cm^{-1}, associated with Si–O–Al symmetric stretching vibrations, is attributed to mullite [40–42].

According to the XRD data, the raw Class C FA (C) and the fine fraction (C-S) contain, in addition to the glass phase, tricalcium aluminate ($Ca_3Al_2O_6$), brownmillerite, anhydrite, calcite, portlandite, CaO, quartz, periclase, and an iron-containing spinel (Figure 6a). It should be noted that, compared with C, the intensities of the quartz reflections in the C-S XRD pattern are substantially lower, consistent with the pronounced decrease in the SiO_2 content of C-S (Table 1). In contrast, the intensities of the reflections of Ca-containing phases—$Ca(OH)_2$, CaO, and $CaSO_4$—in C-S increased relative to those in the raw FA C. These changes are also evident in the FTIR spectra (Figure 6b). The increased portlandite content in C-S is indicated by the higher intensity of the characteristic band of the O–H stretching vibrations in $Ca(OH)_2$ at 3643 cm^{-1} in comparison to that in C. The split band corresponding to the asymmetric stretching vibrations of the SO_4 group in anhydrite at 1147 and 1113 cm^{-1} [43,44] is also more intense in C-S than in C. This confirms the increase in $CaSO_4$ content detected by XRD (Figure 6a) and corresponds to the increase in sulfur oxide content in C-S (Table 1). The bands at 676, 612, and 594 cm^{-1} correspond to the asymmetric bending vibrations of the SO_4 group in anhydrite [43,44]. The doublet at 796 and 775 cm^{-1} is assigned to the symmetric stretching vibrations of Si–O–Si in quartz [40–42].

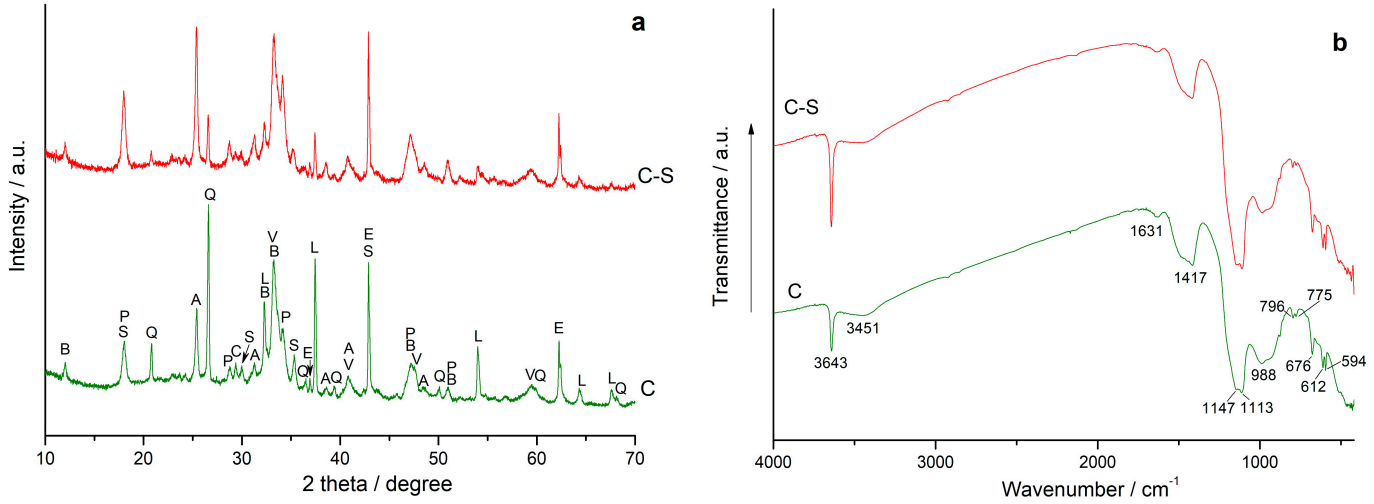

Figure 6. XRD patterns (**a**) and FTIR spectra (**b**) of the raw Class C FA (C) and fine fraction of Class C FA (C-S). The marked phases are: Q—α-quartz (PDF 00-046-1045), B—brownmillerite (PDF 04-015-8023), C—calcite (PDF 01-083-4605), V—tricalcium aluminate $Ca_3Al_2O_6$ (PDF 01-074-7039), A—anhydrite $CaSO_4$ (PDF 00-014-0374), L—lime CaO (PDF 00-037-1497), P—portlandite $Ca(OH)_2$ (PDF 00-04-0733), S—iron-containing spinel $MgAl_{2}Fe_{1.8}O_4$ (PDF 01-071-1233), E—periclase MgO (PDF 00-045-0946).

The broad band with a maximum at 988 cm^{-1} corresponds to the asymmetric stretching vibrations of Si–O–T (T = Si, Al) in the glass phase of high-calcium FA. Compared with the corresponding band of low-calcium FA (Figure 5b), it is shifted toward lower wavenumbers. This apparently indicates that a significant proportion of the silicon atoms in the SiO_4 tetrahedra is substituted by aluminum and, possibly, that the ash C has a lower degree of polymerization than the ash F [41].

The broad band at 1417 cm^{-1} (Figure 6b) corresponds to the asymmetric stretching vibrations of the CO_3^{2-} group. This band is attributed to the chemisorption of atmospheric CO_2 on portlandite [45] and brownmillerite [46] surfaces, as well as to the presence of calcite in C and C-S.

Laser diffraction analysis revealed that 90% of the F-S particles (d_{90}) were smaller than 16.5 μm, while 50% (d_{50}) and 10% (d_{10}) were smaller than 8.8 and 3.5 μm, respectively. C-S exhibited a finer particle-size distribution, with d_{90}, d_{50}, and d_{10} values of 3.8, 1.5, and 0.6 μm, respectively. The specific surface areas were 2.52 m^2/g for F-S and 7.72 m^2/g for C-S. The particle-size and specific-surface-area data are consistent with the SEM images of F-S and C-S presented in Figures 7a and 7b, respectively.

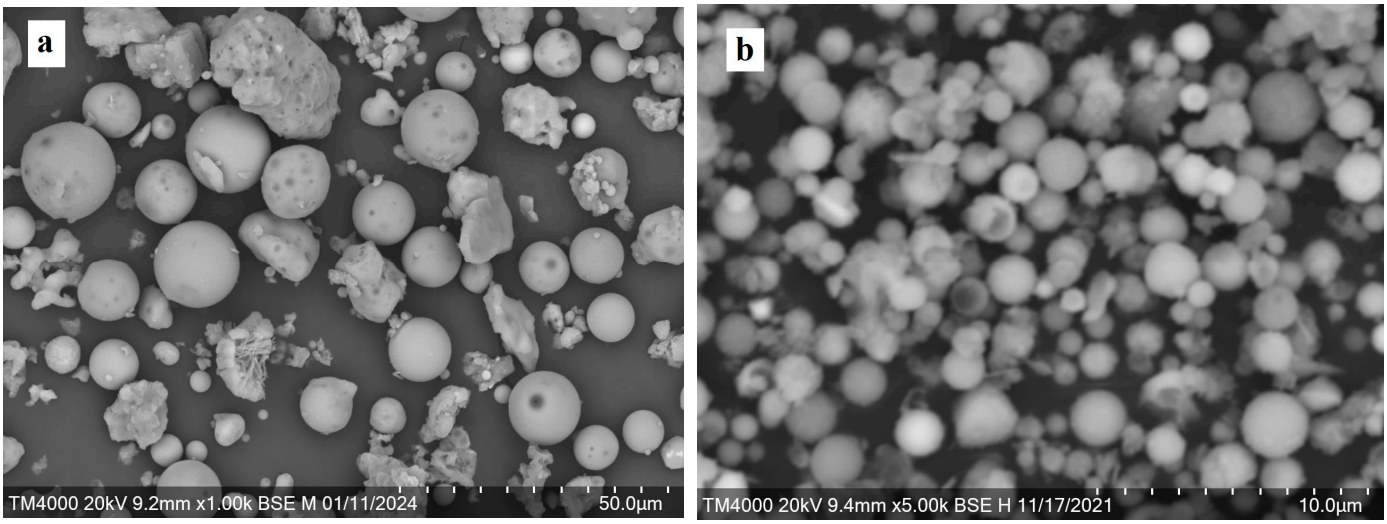

Figure 7. SEM images of F-S (**a**) and C-S (**b**).

3.3. Mechanical Properties of Geopolymers

Figure 8 presents the compressive strength data for geopolymers based on the fine fraction of low-calcium FA (GF-S). For comparison, Figure 8 also shows the strengths of geopolymers produced using the raw low-calcium FA (GF-0) and the same FA mechanically activated for 30 s (GF-30) and 180 s (GF-180) [33]. Compared with GF-0, the geopolymer derived from the fine non-magnetic fraction (GF-S) exhibited a substantial increase in compressive strength—by factors of 5.5, 6.0, and 4.9 after 7, 28, and 180 days of curing, respectively. This enhancement is attributed to the combined effect of several factors resulting from magnetic separation. First, the removal of the magnetic fraction reduced the content of magnetite, which acts largely as an inert filler during alkali activation. Consequently, as shown in Table 1, the relative concentrations of Si and Al—the essential network-forming elements required for geopolymer matrix development—increased in the non-magnetic fraction. Furthermore, the specific surface area S_{sp} of F-S (2.52 m^2/g) is nearly double that of raw fly ash F (1.29 m^2/g), indicating a finer particle size. Together, the higher availability of reactive aluminosilicate phases and the larger surface area significantly enhance the dissolution rate of F-S in the NaOH solution, accelerating geopolymer gel formation compared to the raw fly ash. In terms of mechanical performance, short-term mechanical activation of the raw FA for 30 s (GF-30) yielded approximately the same strength-enhancing effect as utilizing the fine fraction (GF-S). However, extending the milling time to 180 s (GF-180) provided an additional two- to threefold increase in compressive strength (Figure 8).

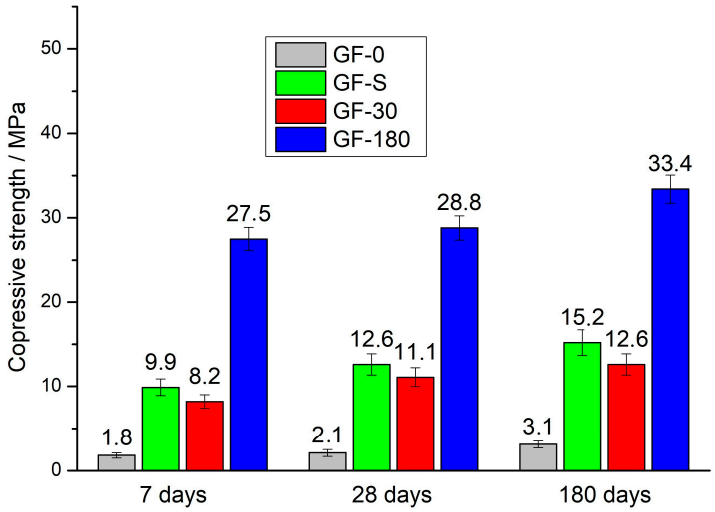

Figure 8. Compressive strength of the geopolymers prepared using the fine fraction of Class F FA (GF-S) at the age of 7, 28 and 180 d. For comparison purposes, compressive strengths of the geopolymers based on a raw low-calcium FA (GF-0) and low-calcium FA mechanically activated for 30 s (GF-30) and 180 s (GF-180) [33] are shown.

The geopolymer based on the fine fraction of Class F FA with the addition of the fine fraction of Class C FA (GF_8C_2-S) showed a significant increase in strength (Figure 9) compared with the geopolymer based on 100% fine fraction of Class F FA (Figure 8). Replacing 20% of the fine Class F FA with the fine Class C FA fraction increased the compressive strength from 9.9 ± 1.0 to 28.5 ± 1.4 MPa (a 2.9-fold increase) at 7 days, from 12.6 ± 1.3 to 30.3 ± 1.5 MPa (2.4-fold) at 28 days, and from 15.2 ± 1.5 to 32.9 ± 1.6 MPa (2.2-fold) at 180 days.

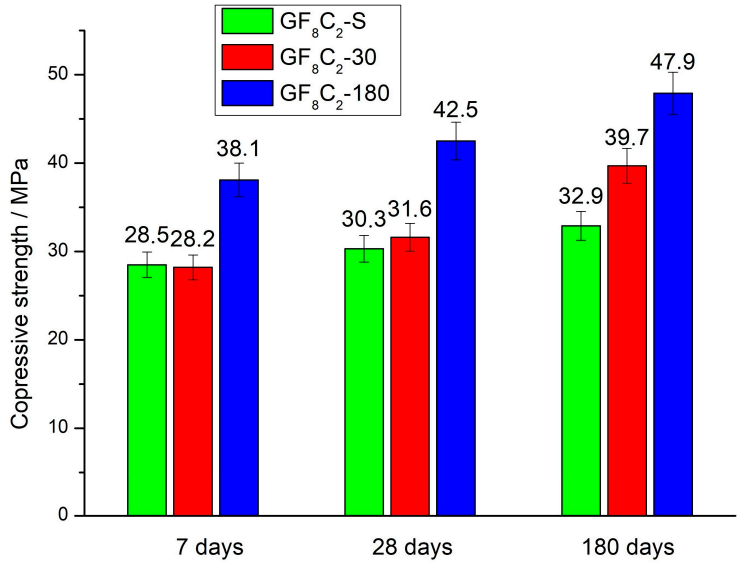

Figure 9. Compressive strength of the geopolymers prepared using the fine fraction of Class F FA blended with fine fraction of Class C FA (GF_8C_2-S) at the age of 7, 28 and 180 d. For comparison purposes, compressive strengths of the geopolymers based on a mixture of 80% Class F FA + 20% Class C FA mechanically activated for 30 s (GF_8C_2-30) and 180 s (GF_8C_2-180) [33] are shown.

It should be noted that this comparison was conducted at a fixed Na_2O/FA ratio rather than a fixed water-to-solid (*w*/*s*) ratio, as the *w*/*s* ratio was adjusted from 0.39 (GF-S)

to 0.37 (GF_8C_2-S) to maintain comparable workability. While a 0.02 reduction in the *w*/*s* ratio (a ~5% decrease) contributes to matrix densification, previous studies indicate that such a minor variation accounts for a strength gain of no more than ~30% [47,48]. Therefore, the slight reduction in *w*/*s* is only a secondary contributing factor and cannot alone explain the substantial 2.4-fold increase in 28-day strength (from 12.6 ± 1.3 MPa for GF-S to 30.3 ± 1.5 MPa for GF_8C_2-S). Instead, the dominant driving force behind this mechanical enhancement is the chemical and phase modification induced by the Class C FA addition. Specifically, the introduction of reactive calcium-bearing phases ($Ca(OH)_2$, free CaO, and $CaSO_4$) promotes the dissolution of aluminosilicate species from the FA particles and accelerates the formation of the primary binding N-A-S-H gel (alongside calcium-modified gel phases) [11].

For GF_8C_2-S (7 and 28 days), in comparison with the geopolymer based on the F and C mixture mechanically activated for 30 s (GF_8C_2-30), as in the case of GF-S and GF-30 (Figure 8), an approximately equal strength is observed. The difference in strength for all curing ages between the geopolymers GF_8C_2-S and GF_8C_2-30, on the one hand, and GF_8C_2-180, on the other (Figure 9), decreased substantially compared with the difference in strength for the analogous geopolymers based on the additive-free low-calcium FA (GF-S and GF-30 versus GF-180, Figure 8). The lower efficiency of extending the milling time to 180 s for the blended-FA geopolymers is likely due to soft mineral phases ($Ca(OH)_2$, calcite, gypsum) in the Class C FA. During co-milling, these phases can shield the class F FA particles, hindering their activation [33].

Notably, the separation of the fine non-magnetic fraction, combined with the addition of the fine fraction of high-calcium FA, increased the GF_8C_2-S geopolymer strength by factors of 15.8 (28.5 ± 1.4 vs. 1.8 ± 0.3 MPa), 14.4 (30.3 ± 1.5 vs. 2.1 ± 0.4 MPa), and 10.6 (32.9 ± 1.6 vs. 3.1 ± 0.4 MPa) at curing ages of 7, 28, and 180 days, respectively, compared to the baseline geopolymer prepared using the raw low-calcium FA (GF-0).

3.4. Characterization of Geopolymers Using XRD, FTIR Spectroscopy and SEM

Figure 10 shows the XRD patterns of the FA mixture (F_8C_2-S) and the geopolymer prepared from this mixture at the age of 28 days (GF_8C_2-S). In the XRD pattern of F_8C_2-S, besides the peaks of quartz, mullite, and hematite that are part of Class F FA, there are peaks of $Ca(OH)_2$ (portlandite), $CaSO_4$ (anhydrite), CaO, and MgO belonging to the high-calcium FA (Figure 6). Comparing the XRD patterns of F_8C_2-S and GF_8C_2-S, it can be seen that the reflections of portlandite, anhydrite, and CaO are absent in the geopolymer XRD pattern. This indicates that during the geopolymerization of F_8C_2-S, unlike the stable quartz, mullite, and hematite, the Ca-containing minerals actively react with the alkaline solution to form new phases.

In the XRD pattern of GF_8C_2-S, an increase in the intensity of the halo in the 25–35° 2θ region is noted, indicating the formation of sodium–(calcium)-containing aluminosilicate hydrogel (N-(C)-A-S-H gel) [49,50], as well as a noticeable increase in the intensity of the main calcite reflection at 2θ ≈ 29.4° (d = 3.036 Å, PDF 01-083-4605). Secondary reflections of calcite are not observed due to their significantly lower relative intensities, while the presence of this phase is independently confirmed by FTIR spectroscopy (Figure 11). Comparison with the ICDD reference stick patterns (Figure 10) confirms that the main calcite peak and the diagnostic reflections of the newly formed crystalline phase—katoite $Ca_3Al_2(SiO_4)(OH)_8$ (PDF 00-038-0368)—are well resolved without overlapping. Katoite is identified qualitatively based on the set of its characteristic reflections shown in Figure 10, indicating the crystallization of this phase during geopolymerization.

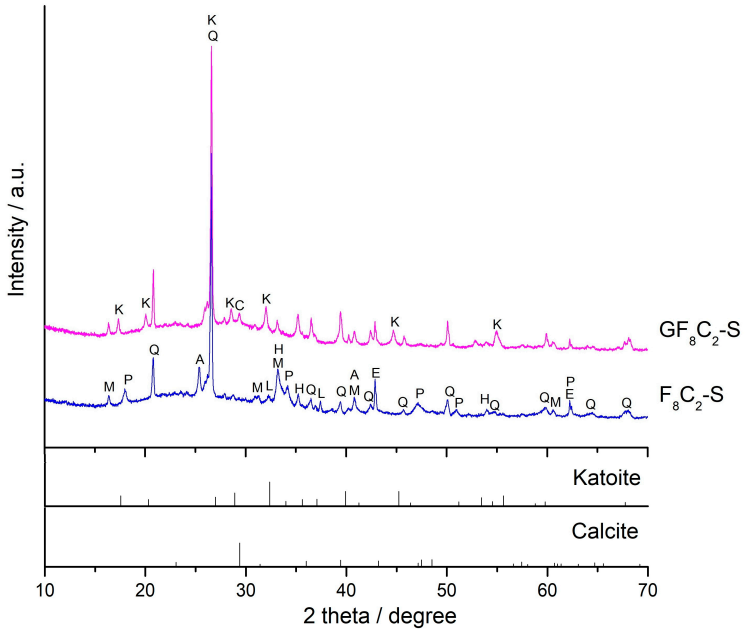

Figure 10. XRD patterns of the fine fraction of Class F FA blended with fine fraction of Class C FA (F_8C_2-S) and the geopolymer prepared using this mixture at the age of 28 d (GF_8C_2-S). The marked phases are: Q—α-quartz (PDF 00-046-1045), C—calcite (PDF 01-083-4605), A—anhydrite $CaSO_4$ (PDF 00-014-0374), L—lime CaO (PDF 00-037-1497), P—portlandite $Ca(OH)_2$ (PDF 00-04-0733), E—periclase MgO (PDF 00-045-0946), K—katoite (PDF 00-038-0368). The reference stick patterns for katoite (PDF 00-038-0368) and calcite (PDF 01-083-4605) are plotted.

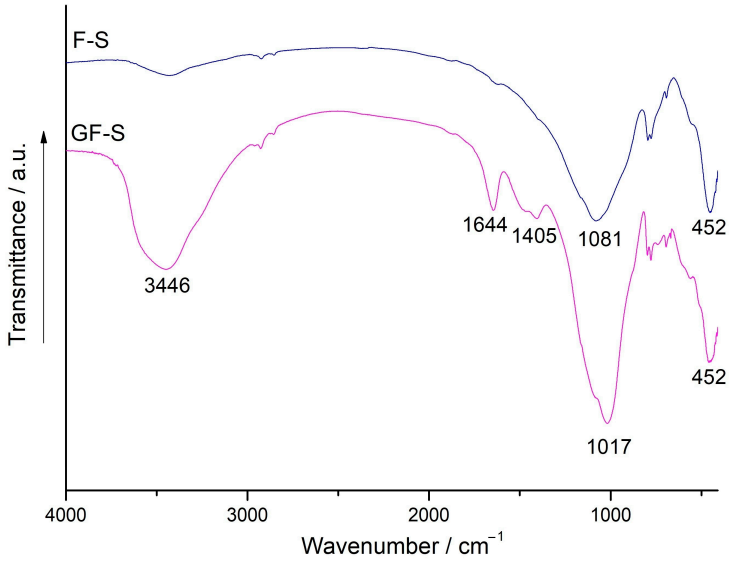

Figure 11. FTIR spectra of the fine fraction of Class F FA (F-S) and the geopolymer prepared using this mixture at the age of 28 d (GF-S).

The increase in calcite content in GF_8C_2-S compared with F_8C_2-S appears to be due to the dissolution of Ca-containing minerals (CaO, anhydrite) in the alkaline solution and their subsequent interaction with atmospheric carbon dioxide during curing. The formation of katoite ($Ca_3Al_2(SiO_4)(OH)_8$, a mineral of the hydrogarnet (hydrogrossular) group [51], was observed during alkaline activation of unblended Class C FAs [52,53] and low-calcium FAs with Ca-containing additives such as $Ca(OH)_2$ [54], Portland cement [55], calcium aluminate cement [56], and $Ca(OH)_2$ + basic oxygen furnace steel slag [57]. Its appearance is directly related to the presence of a sufficient amount of reactive calcium

and aluminum, the source of which in our case is the high-calcium FA, under conditions of elevated temperature or hydrothermal treatment [58]. It should be noted that katoite was not detected in geopolymers based on the mechanically activated mixture (80% FA F + 20% FA C) synthesized under the same curing conditions [33]. This is probably due to the lower content of reactive phases such as portlandite and anhydrite in the raw high-calcium FA (C) compared with C-S (Figure 6).

It can be assumed that the effect of katoite on the mechanical properties of geopolymers is complex in nature. On the one hand, fine katoite crystals may act as a micro-filler that effectively fills the pores of the binding matrix, thereby increasing the strength of the geopolymer. On the other hand, the precipitation of katoite may lead to excessive binding of reactive Al^{3+} and Si^{4+}, competing with the processes of formation of the main aluminosilicate gel. Further research is needed to clarify the role of katoite in alkali activation of FAs (see Section 4, "Limitations").

In the case of geopolymerization of the additive-free low-calcium FA fraction (F-S), the changes are similar to those for mechanically activated low-calcium Class F FA [33]. They include the formation of N-A-S-H gel and a small amount of calcite, which is explained by the reaction of dissolved calcium present in Class F FA (Table 1) with atmospheric CO_2 during curing. The formation of the N-A-S-H gel in GF-S is evidenced by an increased intensity and a shift toward lower wavenumbers of the main Si–O–T (T = Si, Al) asymmetric stretching band in the 1100–1000 cm^{-1} region (Figure 11). In the precursor F-S, this band is located at 1081 cm^{-1}, whereas in GF-S, it shifts to 1017 cm^{-1}, giving a shift magnitude of 64 cm^{-1}. This value falls within the range commonly reported for alkali-activated fly ash-based geopolymers, where the Si–O–T band of the precursor (typically 1100–1060 cm^{-1}) moves up to approximately 1000 cm^{-1} upon geopolymerization [40–42]. These changes can be explained by the substitution of Si by Al in the silicon–oxygen tetrahedra during geopolymerization: because Al–O bonds are weaker and longer than Si–O bonds, the incorporation of Al lowers the force constant of the T–O–T network and thus the vibrational frequency [40–42]. The formation of aluminosilicate hydrogel is also indicated by an increase in the intensity of the bands of O–H stretching vibrations (3446 cm^{-1}) and H–O–H bending vibrations (1644 cm^{-1}) [59] in the GF-S spectrum compared with that in the F-S spectrum [60].

The band at 1405 cm^{-1} in the spectrum of GF-S is attributed to the asymmetric stretching vibrations of the CO_3 group [59]. Its appearance is due to the formation of calcite and, probably, sodium carbonates as a result of the interaction of the unreacted alkaline agent with atmospheric carbon dioxide.

According to the FTIR spectroscopy data, more profound changes occur during alkaline activation of the mixture of fractions (Figure 12) compared with F-S (Figure 11). First, in agreement with the XRD data (Figure 10), the intense band of O–H stretching vibrations at 3641 cm^{-1} characteristic of portlandite, which is present in the FTIR spectrum of F_8C_2-S, completely disappears in the spectrum of GF_8C_2-S. Second, the main Si–O–T stretching band shifts from 1107 cm^{-1} in F_8C_2-S to 1006 cm^{-1} in GF_8C_2-S, a shift magnitude of 101 cm^{-1}. This shift is notably larger than that observed for GF-S (64 cm^{-1}, Figure 11), indicating a higher extent of Al incorporation into the geopolymer network in the blended system. It should be noted, however, that the position of the Si–O–T band is sensitive not only to the bulk Si/Al ratio but also to the local bonding environment and the presence of non-bridging oxygens; therefore, the shift magnitude is interpreted here as a relative indicator of the degree of structural reorganization rather than as a direct quantitative measure of polymerization. The maximum of this band in the spectrum of GF_8C_2-S (1006 cm^{-1}) indicates the formation of N-(C)-A-S-H gel. The analogous bands of C–(A)–S–H and C–S–

H gels are located at 952 and 960 cm^{-1}, respectively [50], and they are absent in the spectrum of GF_8C_2-S. During the alkali activation of F_8C_2-S, the development of these gel phases is presumably restricted to minor amounts, if present at all.

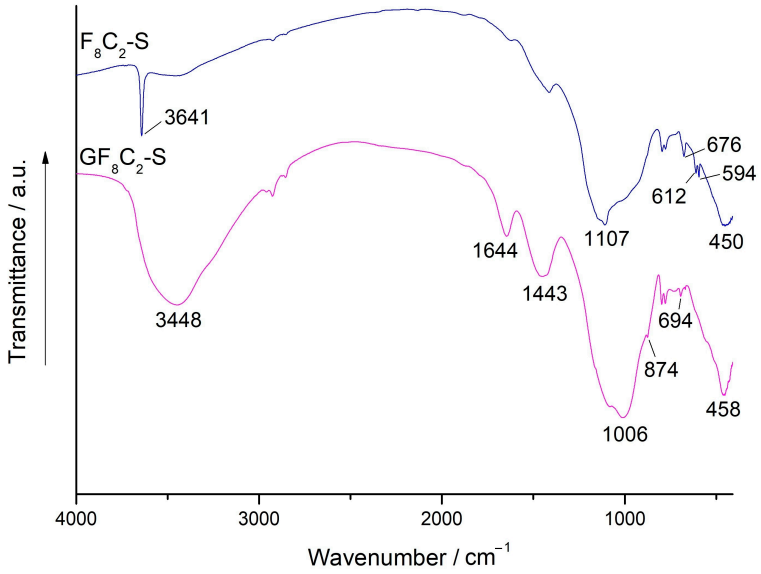

Figure 12. FTIR spectra of the fine fraction of Class F FA blended with fine fraction of Class C FA (F_8C_2-S) and the geopolymer prepared using this mixture at the age of 28 d (GF_8C_2-S).

The precursor spectrum (F_8C_2-S) features bands at 676, 612, and 594 cm^{-1} assigned to the asymmetric bending modes of SO_4^{2-} in anhydrite. Their absence in the GF_8C_2-S geopolymer spectrum correlates with the dissolution of anhydrite observed in the XRD patterns (Figure 10). Furthermore, the absorption bands at 1443 and 874 cm^{-1} correspond, respectively, to the asymmetric stretching and bending vibrations of the CO_3^{2-} ion in calcite [59], which confirms the detection of this crystalline phase in GF_8C_2-S by means of XRD.

Figure 13 shows SEM images of the geopolymers based on F-S and F_8C_2-S at the age of 28 days. Consistent with the strength data (Figures 8 and 9), the geopolymer synthesized from the mixed fractions (Figure 13b) exhibits a more uniform microstructure and fewer unreacted FA microspheres than the additive-free, low-calcium FA (Figure 13a). Higher-magnification images show that GF_8C_2-S (Figure 13d) has a denser microstructure with fewer micropores than GF-S (Figure 13c), which is attributed to the higher reactivity of its precursor and enhanced gel formation.

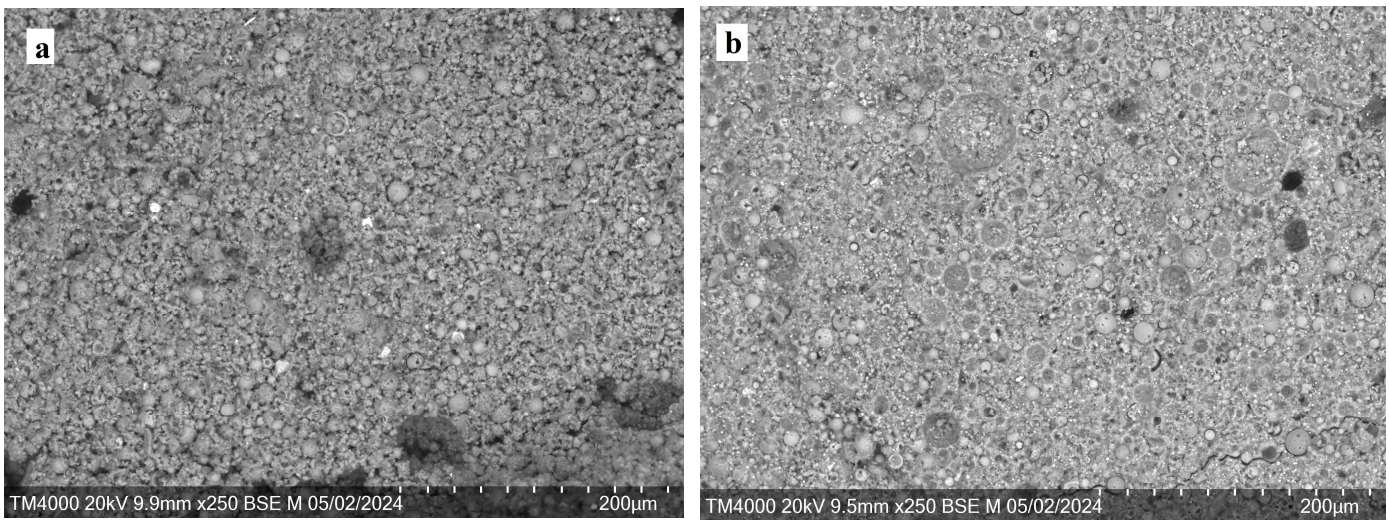

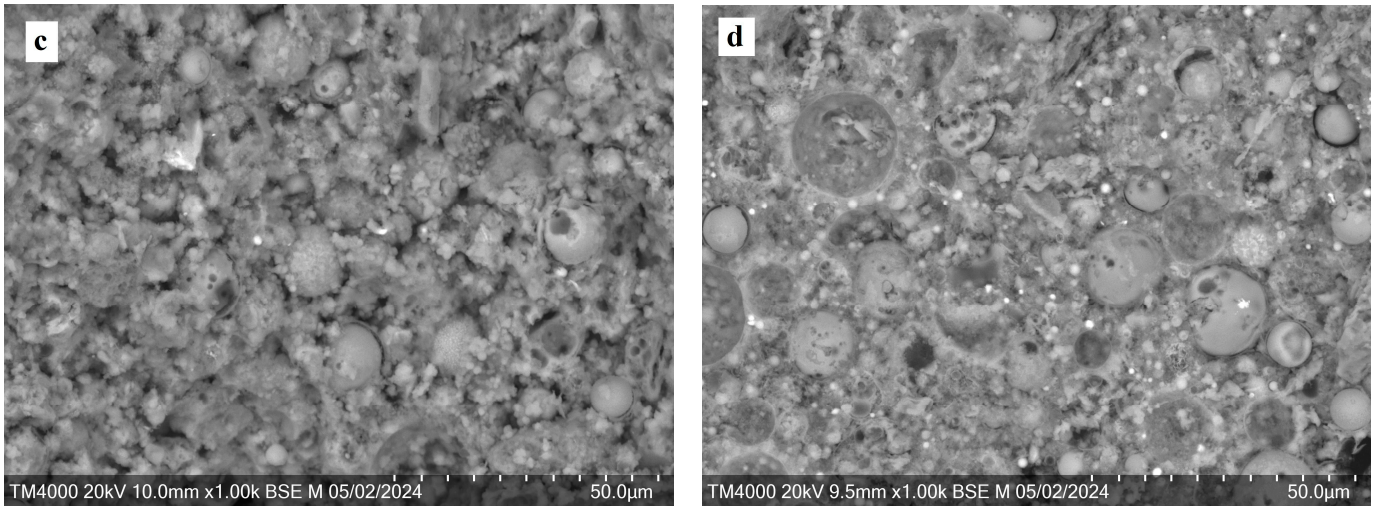

Figure 13. SEM images of the geopolymers synthesized using the fine fraction of Class F FA (**a**,**c**) and the fine fraction of Class F FA blended with the fine fraction of Class C FA (**b**,**d**) at the age of 28 d.

4. Limitations

A limitation of the present study is the inability to quantitatively decouple the exact contribution of katoite to the mechanical performance of the geopolymers. While fine katoite crystals may potentially act as a pore-filling micro-phase, their precipitation simultaneously consumes reactive Al^{3+} and Si^{4+} species, which could compete with the formation of the primary aluminosilicate gel. Determining the net balance between these two opposing effects requires targeted experiments—such as evaluating mechanical strength at a fixed gel content with and without katoite seeding—which remains a subject for future investigation.

5. Conclusions

In this study, geopolymers were synthesized using two precursors: a fine non-magnetic fraction of low-calcium FA (F-S) and a blend of F-S with the fine fraction of high-calcium FA at an 8:2 ratio (F_8C_2-S). The processes occurring during precursor activation with a sodium hydroxide solution and their effects on geopolymer strength were investigated. The results were also compared with those obtained previously for geopolymers based on mechanically activated counterparts of the same raw class F and class C FAs.

The main findings of this study include the following:

1. Utilizing the fine non-magnetic fraction of Class F FA (GF-S) increased compressive strength by 5.5-, 6.0-, and 4.9-fold relative to the raw Class F FA reference (GF-0) at 7, 28, and 180 days, respectively (reaching 12.6 ± 1.3 MPa at 28 days). Brief planetary milling of the raw FA for 30 s (GF-30) yielded comparable strengths within experimental error at 7 days (8.2 ± 0.8 MPa) and 28 days (11.1 ± 1.1 MPa), whereas at 180 days, the fractionated GF-S geopolymer achieved a somewhat higher strength (15.2 ± 1.5 vs. 12.6 ± 1.3 MPa).
2. Substituting 20% of the fine Class F FA fraction with the fine Class C FA fraction (GF_8C_2-S) yielded 2.9-, 2.4-, and 2.2-fold higher compressive strength than the unblended GF-S geopolymer at 7, 28, and 180 days of curing, respectively, achieving a 28-day strength of 30.3 ± 1.5 MPa (and reaching 32.9 ± 1.6 MPa at 180 days). Relative to the raw Class F FA reference (GF-0), this blended formulation demonstrated a remarkable overall strength increase by factors of 15.8, 14.4, and 10.6 at 7, 28, and 180 days, respectively. Furthermore, similar to the Class C-free system, 30-s mechanical

activation (GF_8C_2-30) produced 7- and 28-day compressive strengths comparable to those of the fractionated GF_8C_2-S blend.

3. XRD and FTIR analyses revealed that an N-(C)-A-S-H gel constituted the main binding matrix in both GF-S and GF_8C_2-S. The introduction of the high-calcium FA fraction accelerated gel synthesis and promoted the formation of a new crystalline phase, katoite, $Ca_3Al_2(SiO_4)(OH)_8$. According to the SEM results, enhanced gel formation led to the development of a denser, more homogeneous matrix structure, accounting for the observed improvement in compressive strength.
4. The findings show that the proposed method yields geopolymers with strengths comparable to those of geopolymers produced from mechanically activated FA mixtures without fractionation. Since the magnetic fraction of FA F can be redirected to metallurgy, the coarse non-magnetic fraction can be selectively milled to the desired fineness. This strategy avoids the intensive milling step while maintaining key operational characteristics, promoting a more efficient, integrated approach to FA utilization. The magnetic fraction obtained by dry magnetic separation has an iron content, expressed as Fe_2O_3, of 56 wt % (compared with 8.7 wt % in the initial fly ash and 5 4 wt.% in the non-magnetic fraction), with magnetite as the predominant iron-bearing phase confirmed by XRD. The iron recovery to this fraction was approximately 42%, indicating that a substantial proportion of the total iron reported to the magnetic product. These results confirm that dry magnetic separation effectively produces a magnetite-rich fraction, while the non-magnetic fraction serves as a geopolymer precursor.

Author Contributions: Conceptualization, A.M.K., E.V.F.; methodology, A.M.K., E.V.F., E.V.K.; formal analysis and investigation, E.V.K., E.A.K., A.G.I., G.V.A.; writing—original draft preparation, A.M.K., E.V.F.; writing—review and editing, A.M.K., E.V.F., E.V.K. All authors have read and agreed to the published version of the manuscript.

Funding: This research received no external funding.

Data Availability Statement: Data are contained within the article.

Acknowledgments: This research was conducted within the framework of the budget projects FMEZ-2025-0059 for the Tananaev Institute of Chemistry of the Federal Research Centre of Kola Science Centre of the Russian Academy of Sciences and FWES 2026–0011 for the Institute of Chemistry and Chemical Technology of the Siberian Branch of the Russian Academy of Sciences, using the equipment of Krasnoyarsk Regional Research Equipment Centre of the Siberian Branch of the Russian Academy of Sciences for the SEM–EDS study.

Conflicts of Interest: The authors declare no conflicts of interest.

Abbreviations

The following abbreviations are used in this manuscript:

FA	Fly ash
F	Raw low-calcium FA
C	Raw high-calcium FA
F-S	Fine non-magnetic fraction of low-calcium fly ash F
F-MF-S	Fine magnetic fraction of low-calcium fly ash F
C-S	Fine fraction of high-calcium fly ash C
F_8C_2-S	Precursor prepared using 80% F-S and 20% C-S
RH	Relative humidity
GF-S	Geopolymer prepared using F-S
GF_8C_2-S	Geopolymer prepared using F_8C_2-S
GF-0	Geopolymer prepared using raw low-calcium fly ash F

GF-30	Geopolymer prepared in [33] using low-calcium fly ash F milled for 30 s
GF-180	Geopolymer prepared in [33] using low-calcium fly ash F milled for 180 s
GF_8C_2-30	Geopolymer prepared in [33] using (80% F + 20% C) milled for 30 s
GF_8C_2-180	Geopolymer prepared in [33] using (80% F + 20% C) milled for 180 s

References

1. Yao, Z.T.; Ji, X.S.; Sarker, P.K.; Tang, J.H.; Ge, L.Q.; Xia, M.S.; Xi, Y.Q. A comprehensive review on the applications of coal fly ash. *Earth-Sci. Rev.* **2015**, *141*, 105–121. https://doi.org/10.1016/j.earscirev.2014.11.016.
2. Davidovits, J. Geopolymers: Inorganic polymeric new materials. *J. Therm. Anal. Calorim.* **1991**, *37*, 1633–1656. https://doi.org/10.1007/BF01912193.
3. Duxson, P.; Fernández-Jiménez, A.; Provis, J.L.; Lukey, G.C.; Palomo, A.; van Deventer, J.S.J. Geopolymer technology: The current state of the art. *J. Mater. Sci.* **2007**, *42*, 2917–2933. https://doi.org/10.1007/s10853-006-0637-z.
4. Singh, N.B.; Middendorf, B. Geopolymers as an alternative to Portland cement: An overview. *Constr. Build. Mater.* **2020**, *237*, 117455. https://doi.org/10.1016/j.conbuildmat.2019.117455.
5. Li, Z.; Xu, G.; Shi, X. Reactivity of coal fly ash used in cementitious binder systems: A state-of-the-art overview. *Fuel* **2021**, *301*, 121031. https://doi.org/10.1016/j.fuel.2021.121031.
6. Hadi, M.N.; Al-Azzawi, M.; Yu, T. Effects of fly ash characteristics and alkaline activator components on compressive strength of fly ash-based geopolymer mortar. *Constr. Build. Mater.* **2018**, *175*, 41–54. https://doi.org/10.1016/j.conbuildmat.2018.04.092.
7. Kalombe, R.M.; Ojumu, V.T.; Eze, C.P.; Nyale, S.M.; Kevern, J.; Petrik, L.F. Fly ash-based geopolymer building materials for green and sustainable development. *Materials* **2020**, *13*, 5699. https://doi.org/10.3390/ma13245699.
8. Winnefeld, F.; Leemann, A.; Lucuk, M.; Svoboda, P.; Neuroth, M. Assessment of phase formation in alkali activated low and high calcium fly ashes in building materials. *Constr. Build. Mater.* **2010**, *24*, 1086–1093. https://doi.org/10.1016/j.conbuildmat.2009.11.007.
9. Guo, X.; Shi, H.; Dick, W.A. Compressive strength and microstructural characteristics of class C fly ash geopolymer. *Cem. Concr. Compos.* **2010**, *32*, 142–147. https://doi.org/10.1016/j.cemconcomp.2009.11.003.
10. Kaya, M.; Uysal, M.; Yilmaz, K.; Karahan, O.; Atiş, C.D. Mechanical properties of class C and F fly ash geopolymer mortars. *Gradevinar* **2020**, *72*, 297–309. https://doi.org/10.14256/JCE.2421.2018.
11. Canfield, G.M.; Eichler, J.; Griffith, K.; Hearn, J.D. The role of calcium in blended fly ash geopolymers. *J. Mater. Sci.* **2014**, *49*, 5922–5933. https://doi.org/10.1007/s10853-014-8307-z.
12. Nuaklong, P.; Wongsa, A.; Sata, V.; Boonserm, K.; Sanjayan, J.; Chindaprasirt, P. Properties of high-calcium and low-calcium fly ash combination geopolymer mortar containing recycled aggregate. *Heliyon* **2019**, *5*, e02513. https://doi.org/10.1016/j.heliyon.2019.e02513.
13. Sharonova, O.M.; Yumashev, V.V.; Dobrosmyslov, S.S. Production and properties of geopolymer binders based on high-calcium fly ash. *J. Sib. Fed. Univ. Chem.* **2025**, *18*, 476–487.
14. Toobpeng, N.; Thavorniti, P.; Jiemsirilers, S. Effect of additives on the setting time and compressive strength of activated high-calcium fly ash-based geopolymers. *Constr. Build. Mater.* **2024**, *417*, 135035. https://doi.org/10.1016/j.conbuildmat.2024.135035.
15. Chindaprasirt, P.; Chareerat, T.; Sirivivatnanon, V. Workability and strength of coarse high calcium fly ash geopolymer. *Cem. Concr. Compos.* **2007**, *29*, 224–229. https://doi.org/10.1016/j.cemconcomp.2006.11.002.
16. Mohamed, R.; Abd Razak, R.; Al Bakri Abdullah, M.M.; Sofri, L.A.; Aziz, I.H.; Shahedan, N.F. Setting time and after setting properties of high calcium fly ash geopolymers with different concentration of sodium hydroxide. *Arch. Metall. Mater.* **2022**, *67*, 563–567. https://doi.org/10.24425/amm.2022.137791.
17. Nath, S.K.; Maitra, S.; Mukherjee, S.; Kumar, S. Microstructural and morphological evolution of fly ash based geopolymers. *Constr. Build. Mater.* **2016**, *111*, 758–765. https://doi.org/10.1016/j.conbuildmat.2016.02.106.
18. Provis, J.L.; Bernal, S.A. Binder chemistry—Blended systems and intermediate Ca content. In *Alkali Activated Materials: State-of-the-Art Report*; Provis, J.L., van Deventer, J.S.J., Eds.; RILEM TC 224-AAM; Springer: Dordrecht, The Netherlands, 2014; Volume 13, pp. 125–144. https://doi.org/10.1007/978-94-007-7672-2_5.
19. Kumar, R.; Kumar, S.; Alex, T.C.; Singla, R. Mapping of calorimetric response for the geopolymerisation of mechanically activated fly ash. *J. Therm. Anal. Calorim.* **2019**, *136*, 1117–1133. https://doi.org/10.1007/s10973-018-7736-3.
20. Tchadjie, L.; Ekolu, S. Enhancing the reactivity of aluminosilicate materials toward geopolymer synthesis. *J. Mater. Sci.* **2018**, *53*, 4709–4733. https://doi.org/10.1007/s10853-017-1907-7.

21. Kato, K.; Xin, Y.; Hitomi, T.; Shirai, T. Surface modification of fly ash by mechano-chemical treatment. *Ceram. Int.* **2019**, *45*, 849–853. https://doi.org/10.1016/j.ceramint.2018.09.254.
22. Grabias-Blicharz, E.; Franus, W. A critical review on mechanochemical processing of fly ash and fly ash-derived materials. *Sci. Total Environ.* **2023**, *860*, 160529. https://doi.org/10.1016/j.scitotenv.2022.160529.
23. Kalinkin, A.M.; Nath, S.K.; Kalinkina, E.V.; Kumar, S. Geopolymerization of coal fly ash: Effect of milling and mechanical activation. In *Managing Mining and Minerals Processing Wastes*; Qi, C., Benson, C.H., Eds.; Elsevier: Amsterdam, The Netherlands, 2023; pp. 189–208. https://doi.org/10.1016/B978-0-323-91283-9.00009-2.
24. Chindaprasirt, P.; Rattanasak, U. Calcium wastes as an additive for a low calcium fly ash geopolymer. *Sci. Rep.* **2023**, *13*, 16351. https://doi.org/10.1038/s41598-023-43586-w.
25. Kaja, A.M.; Lazaro, A.; Yu, Q.L. Effects of Portland cement on activation mechanism of class F fly ash geopolymer cured under ambient conditions. *Constr. Build. Mater.* **2018**, *189*, 1113–1123. https://doi.org/10.1016/j.conbuildmat.2018.09.065.
26. Li, X.; Chu, Z.; Zhu, G.; Yu, T.; Su, H.; Shao, Y.; Li, X.; Jiang, Z.; Jiao, Z. Freeze–thaw resistance of class C/class F fly ash geopolymer mortars with different ash-to-sand ratios. *Buildings* **2026**, *16*, 1288. https://doi.org/10.3390/buildings16071288.
27. Kumar, S.; Kristály, F.; Mucsi, G. Geopolymerisation behaviour of size fractioned fly ash. *Adv. Powder Technol.* **2015**, *26*, 24–30. https://doi.org/10.1016/j.apt.2014.09.001.
28. Nath, S.K.; Kumar, S. Role of particle fineness on engineering properties and microstructure of fly ash derived geopolymer. *Constr. Build. Mater.* **2020**, *233*, 117294. https://doi.org/10.1016/j.conbuildmat.2019.117294.
29. Xu, X.; Bao, S.; Guo, Z.; Tian, X. A clean approach to high-strength fly ash-based geopolymers: Multi-granular screening with NaAlO2 enhancement. *J. Clean. Prod.* **2024**, *464*, 142733. https://doi.org/10.1016/j.jclepro.2024.142733.
30. Chindaprasirt, P.; Chareerat, T.; Hatanaka, S.; Cao, T. High-strength geopolymer using fine high-calcium fly ash. *J. Mater. Civ. Eng.* **2011**, *23*, 264–270. https://doi.org/10.1061/(ASCE)MT.1943-5533.0000161.
31. van Riessen, A.; Chen-Tan, N. Beneficiation of Collie fly ash for synthesis of geopolymer: Part 1—Beneficiation. *Fuel* **2013**, *106*, 569–575. https://doi.org/10.1016/j.fuel.2012.11.070.
32. van Riessen, A.; Chen-Tan, N. Beneficiation of Collie fly ash for synthesis of geopolymer Part 2—Geopolymers. *Fuel* **2013**, *111*, 829–835. https://doi.org/10.1016/j.fuel.2013.04.015.
33. Kalinkin, A.M.; Fomenko, E.V.; Kalinkina, E.V.; Kruglyak, E.A.; Ivanova, A.G.; Akimochkina, G.V.; Yumashev, V.V. Recycling of low-calcium coal fly ash into environmentally sustainable geopolymer material: Effect of blending with very high-calcium fly ash and mechanical activation. *J. Therm. Anal. Calorim.* **2026**, *151*, 12207–12221. https://doi.org/10.1007/s10973-026-15732-9.
34. Bartoňová, L.; Kovár, F.; Kucbel, M. Magnetic separation of ash and slag residues for their multi-component utilization: An overview. *Int. J. Coal Sci. Technol.* **2025**, *12*, 78. https://doi.org/10.1007/s40789-025-00814-0.
35. Fomenko, E.V.; Akimochkina, G.V.; Anshits, A.G. Narrow dispersed fractions of high-calcium fly ash produced from the pulverized combustion of Irsha-Borodinsky coal. *Therm. Eng.* **2019**, *66*, 560–568. https://doi.org/10.1134/S0040601519080020.
36. Shilaev, V. P. Fundamentals of mineral processing. In *A textbook for Universities*; Nedra: Moscow, Russia, 1986; p. 296.
37. Shoppert, A.; Valeev, D.; Loginova, I.; Chaikin, L.; Pan, J. Enhanced Coal Fly Ash Desilication Using Atmospheric NaOH Leaching with Simultaneous Magnetic Separation. *Metals* **2023**, *13*, 1647. https://doi.org/10.3390/met13101647.
38. Zhang, Z.; Zhu, Q.; Huang, G.; Chen, Y.; Li, J.; Zhao, G.; Peng, X.; Li, J.; Wang, X. Innovative dry magnetic separation for Enhanced recovery of magnetic iron oxides from coal fly ash. *Fuel* **2025**, *388*, 134489. https://doi.org/10.1016/j.fuel.2025.134489.
39. Valeev, D.; Kunilova, I.; Alpatov, A.; Varnavskaya, A.; Ju, D. Magnetite and Carbon Extraction from Coal Fly Ash Using Magnetic Separation and Flotation Methods. *Minerals* **2019**, *9*, 320. https://doi.org/10.3390/min9050320.
40. Fernández-Jiménez, A.; Palomo, A. Mid-infrared spectroscopic studies of alkali-activated fly ash structure. *Microporous Mesoporous Mater.* **2005**, *86*, 207–214. https://doi.org/10.1016/j.micromeso.2005.05.057.
41. Lee, W.K.W.; van Deventer, J.S.J. Use of infrared spectroscopy to study geopolymerization of heterogeneous amorphous aluminosilicates. *Langmuir* **2003**, *19*, 8726–8734. https://doi.org/10.1021/la026127e.
42. Álvarez-Ayuso, E.; Querol, X.; Plana, F.; Alastuey, A.; Moreno, N.; Izquierdo, M.; Font, O.; Moreno, T.; Diez, S.; Vázquez, E.; et al. Environmental, physical and structural characterisation of geopolymer matrixes synthesised from coal (co-)combustion fly ashes. *J. Hazard. Mater.* **2008**, *154*, 175–183. https://doi.org/10.1016/j.jhazmat.2007.10.008.
43. Bishop, J.L.; Lane, M.D.; Dyar, M.D.; King, S.J.; Brown, A.J.; Swayze, G.A. Spectral properties of Ca-sulfates: Gypsum, bassanite, and anhydrite. *Am. Mineral.* **2014**, *99*, 2105–2115. https://doi.org/10.2138/am-2014-4756.
44. Yin, Y.; Yin, J.; Zhang, W.; Tian, H.; Hu, Z.; Ruan, M.; Xu, H.; Liu, L.; Yan, X.; Chen, D. FT-IR and micro-Raman spectroscopic characterization of minerals in high-calcium coal ashes. *J. Energy Inst.* **2018**, *91*, 389–396. https://doi.org/10.1016/j.joei.2017.02.003.

45. Kalinkin, A.M.; Kalinkina, E.V.; Zalkind, O.A.; Makarova, T.I. Chemical interaction of calcium oxide and calcium hydroxide with CO2 during mechanical activation. *Inorg. Mater.* **2005**, *41*, 1073–1079. https://doi.org/10.1007/s10789-005-0263-1.
46. Noori, Z.; Malekzadeh, A.; Poater, J. Brownmillerite calcium ferrite, a promising perovskite-related material in the degradation of a tight dye under ambient conditions. *ChemistryOpen* **2024**, *13*, e202300169. https://doi.org/10.1002/open.202300169.
47. Patankar, S.V.; Jamkar, S.S.; Ghugal, Y.M. Effect of water-to-geopolymer binder ratio on the production of fly ash based geopolymer concrete. *Int. J. Adv. Technol. Civ. Eng.* **2013**, *2*, 79–83.
48. Pham, T.-T.; Nguyen, N.-L.; Nguyen, T.-T.; Nguyen, T.-T.; Pham, T.-H. Effects of superplasticizer and water–binder ratio on mechanical properties of one-part alkali-activated geopolymer concrete. *Buildings* **2023**, *13*, 1835. https://doi.org/10.3390/buildings13071835.
49. de Vargas, A.S.; Dal Molin, D.C.; Masuero, Â.B.; Vilela, A.C.; Castro-Gomes, J.; de Gutierrez, R.M. Strength development of alkali-activated fly ash produced with combined NaOH and $Ca(OH)_2$ activators. *Cem. Concr. Compos.* **2014**, *53*, 341–349. https://doi.org/10.1016/j.cemconcomp.2014.06.012.
50. García-Lodeiro, I.; Palomo, A.; Fernández-Jiménez, A.; Macphee, D.E. Compatibility studies between NASH and CASH gels. Study in the ternary diagram Na_2O–CaO–Al_2O_3–SiO_2–H_2O. *Cem. Concr. Res.* **2011**, *41*, 923–931. https://doi.org/10.1016/j.cemconres.2011.05.006.
51. Passaglia, E.; Rinaldi, R. Katoite, a new member of the $Ca_3Al_2(SiO_4)_3$–$Ca_3Al_2(OH)_{12}$ series and a new nomenclature for the hydrogrossular group of minerals. *Bull. Minéral.* **1984**, *107*, 605–618. https://doi.org/10.3406/bulmi.1984.7804.
52. Mondal, S.K.; Welz, A.; Rezaei, F.; Kumar, A.; Okoronkwo, M.U. Structure–property relationship of geopolymers for aqueous Pb removal. *ACS Omega* **2020**, *5*, 21689–21699. https://doi.org/10.1021/acsomega.0c02591.
53. Kashosi, C.; Gheni, A.; Gomaa, E.; ElGawady, M. Effects of rest time and curing regime on short- and long-term strength of class C fly ash-based alkali-activated mortars. *Materials* **2024**, *17*, 1632. https://doi.org/10.3390/ma17071632.
54. Williams, P.J.; Biernacki, J.J.; Walker, L.R.; Meyer, H.M.; Rawn, C.J.; Bai, J. Microanalysis of alkali-activated fly ash–CH pastes. *Cem. Concr. Res.* **2002**, *32*, 963–972. https://doi.org/10.1016/S0008-8846(02)00734-2.
55. Moon, J.; Wang, Z.; Kim, M.O.; Chun, S.C. Strength enhancement of alkaline activated fly ash cured at ambient temperature by delayed activation of substituted OPC. *Constr. Build. Mater.* **2016**, *122*, 659–666. https://doi.org/10.1016/j.conbuildmat.2016.06.111.
56. Pyatina, T.; Sugama, T.; Moon, J.; James, S. Effect of tartaric acid on hydration of a sodium-metasilicate-activated blend of calcium aluminate cement and fly ash F. *Materials* **2016**, *9*, 422. https://doi.org/10.3390/ma9060422.
57. Zhao, Z.; Qu, X.; Li, F.; Wei, J. Effects of steel slag and silica fume additions on compressive strength and thermal properties of lime-fly ash pastes. *Constr. Build. Mater.* **2018**, *183*, 439–450. https://doi.org/10.1016/j.conbuildmat.2018.05.220.
58. Hou, X.; Ma, S.; Wang, X.; Liu, R.; Ibrahim, M. Hydrothermal transformation of fly ash to tobermorite or katoite: Impact of Ca and Si concentration in the liquid phase without alkali activation. *Ceram. Int.* **2024**, *50*, 17291–17301. https://doi.org/10.1016/j.ceramint.2024.02.210.
59. Nakamoto, K. *Infrared and Raman Spectra of Inorganic and Coordination Compounds: Part A: Theory and Applications in Inorganic Chemistry*, 5th ed.; Wiley: New York, NY, USA, 1997; p. 387.
60. Rozek, P.; Krol, M.; Mozgawa, W. Spectroscopic studies of fly ash-based geopolymers. *Spectrochim. Acta Part A Mol. Biomol. Spectrosc.* **2018**, *198*, 283–289. https://doi.org/10.1016/j.saa.2018.03.034.

Disclaimer/Publisher's Note: The statements, opinions and data contained in all publications are solely those of the individual author(s) and contributor(s) and not of MDPI and/or the editor(s). MDPI and/or the editor(s) disclaim responsibility for any injury to people or property resulting from any ideas, methods, instructions or products referred to in the content.